

Supplementary Information

Stabilizing Atomic Pt with Trapped Interstitial F in Alloyed PtCo Nanosheets for High-Performance Zinc-Air Battery

Zhao Li^{1,2,#}, Wenhan Niu^{2,#}, Zhenzhong Yang^{3,#}, Nusaiba Zaman⁴, Widitha Samarakoon⁵, Maoyu Wang⁵, Abdelkader Kara⁴, Marcos Lucero⁵, Manasi V. Vyas⁵, Hui Cao⁶, Hua Zhou⁷, George E. Sterbinsky⁷, Zhenxing Feng^{5,*}, Yingge Du^{3,*}, and Yang Yang^{1,2,8,*}

¹Department of Materials Science and Engineering, University of Central Florida, Orlando, FL 32826, United States

²NanoScience Technology Center, University of Central Florida, Orlando, FL 32826, United States

³Physical and Computational Sciences Directorate, Pacific Northwest National Laboratory, Richland, Washington 99352, United States

⁴Department of Physics, University of Central Florida, Orlando, FL 32826, United States

⁵School of Chemical, Biological, and Environmental Engineering, Oregon State University, Corvallis, OR 97331, United States

⁶Materials Science Division, Argonne National Laboratory, Lemont, IL 60439, United States

⁷X-ray Science Division, Argonne National Laboratory, Lemont, IL 60439, United States

⁸Energy Conversion and Propulsion Cluster, University of Central Florida, Orlando, FL 32826, United States

*Email: Yang.Yang@ucf.edu; Yingge.Du@pnnl.gov; zhenxing.feng@oregonstate.edu

#These authors contributed equally to this work.

Experimental Section

Chemicals: Potassium hydroxide (KOH, $\geq 85\%$, Sigma-Aldrich), ethanol anhydrous (C_2H_5OH , Fisher Chemical), isopropanol (C_3H_8O , extra pure, Acros Organics), cobalt (II) sulfate heptahydrate ($CoSO_4 \cdot 7H_2O$, 98%, Alfa Aesar), boric acid (H_3BO_3 , $\geq 99.5\%$, Fisher Chemical), dihydrogen hexachloroplatinate (IV) hydrate ($H_2PtCl_6 \cdot 7H_2O$, $\geq 99.9\%$, Alfa Aesar), sodium citrate dihydrate ($Na_3C_6H_5O_7 \cdot 2H_2O$, granular certified, Sigma-Aldrich), sodium dodecyl sulfate ($C_{12}H_{25}NaO_4S$, $>99\%$, Biosciences), zinc acetate ($CH_3COO)_2Zn$, 99%, Acros Organics), poly(vinyl alcohol) (C_2H_4O , 98-99%, Alfa Aesar), Ruthenium oxide powder (RuO_2 , 99%, Sigma-Aldrich), platinum on carbon (Pt/C, 10 wt% loading, Sigma-Aldrich), carbon cloth and carbon paper (Fuel Cell Earth) were used as received. Deionized water (DI water, $18.2 M\Omega \cdot cm$) was used for all aqueous solutions.

Electrochemical fabrication of PtCo with different Pt loading content: Firstly, $CoSO_4 \cdot 7H_2O$, H_3BO_3 , $Na_3C_6H_5O_7 \cdot 2H_2O$, and $C_{12}H_{25}NaO_4S$ were mixed into DI water and stirred for 10 min. Then, a different concentration of $H_2PtCl_6 \cdot 7H_2O$ aqueous solution (0, 0.5, 2, and 3 mM) was added into the mixed-salt solution and stirred for 5 min. The electrodeposition was carried out by using the nickel foam as a cathode and platinum mesh as an anode under the constant current of 0.1 A for 1 h. Finally, a series of PtCo alloy nanosheets prepared by different concentrations of Pt precursor were vertically deposited on the nickel foam, which was further washed with DI water, C_2H_5OH , C_3H_8O and dried at room temperature.

Electrochemical fabrication of SA-PtCoF and control samples: The as-prepared PtCo by 0.5 mM, 2 mM, and 3 mM $\text{H}_2\text{PtCl}_6 \cdot 7\text{H}_2\text{O}$ supported on the nickel foam was exposed to a fluorine (F)-plasma treatment with carbon tetrafluoride (CF_4) as the main source in a plasma etcher (Trion MiniLock II RIE-ICP) for 30 min under the pressure of 150 mT. Then, AP-PtCoF, SA-PtCoF, NC-PtCoF, and CoF catalyst were fabricated and the corresponding weight percentage of Pt was 1.85 wt%, 5.87 wt%, 6.21 wt%, and 0 wt%, respectively. The Pt : Co ratios were measured by X-ray fluorescence spectrometer.

Fabrication of Pt/C@RuO₂: The Pt/C@RuO₂ control sample was prepared by mixing RuO₂ and Pt/C powder in the DI water/Nafion/isopropanol solution at the same loading mass as that of SA-PtCoF (420 $\mu\text{g cm}^{-2}$), which was then ultrasonicated for 30 min. The homogeneous suspension was dispersed on the nickel foam and dried in the oven at 60 °C for 1 h.

Materials characterizations: The morphology, atomic structure, and composition were characterized by scanning electron microscopy (SEM, ZEISS ultra 55) and high-resolution transmission electron microscope (HRTEM) with energy-dispersive X-ray spectroscopy (EDS) mapping (Cs-corrected JEM ARM200F STEM). X-ray diffraction (XRD) pattern was recorded by a film XRD system (Panalytical X'celerator multi-element detector with Cu K α radiation source, $\lambda=1.54056 \text{ \AA}$). The chemical states of elements were detected by X-ray photoelectron spectroscopy (XPS, PHI Quantera, Physical Electronics). The instrumental resolution is 0.025 - 0.1 eV. The Al anode at 25 W is employed as the X-ray source and the pass energy is 26 eV. X-ray absorption spectroscopy (XAS) measurements were performed at beamline 20-BM and 9-BM at Advanced Photon Source, Argonne National Laboratory. Co K-edge and Pt L₃-edge X-ray absorption near

edge structure (XANES) and extended X-ray absorption fine structure (EXAFS) data were collected in transmission mode and fluorescence mode, respectively. Background subtraction and normalization were performed with Athena software package and EXAFS fitting was performed using Artemis software package. Raman spectrum was tested via Renishaw InVia Microscope Raman with 532 nm laser.

Electrochemical characterizations: All the electrochemical measurements were detected by the electrochemical station (CHI 760E) in a standard three-electrode cell with Ag/AgCl (1 M KCl) electrode as the reference, carbon rod as the counter electrode, and the as-prepared catalyst attached on rotating disk electrode (RDE) as the working electrode. All the measured potentials vs the Ag/AgCl reference electrode were converted to reversible hydrogen electrode (RHE) by the Nernst equation $E_{\text{RHE}} = E_{\text{Ag/AgCl}} + 0.059 \text{ pH} + 0.222$. All the OER polarization curves were *iR*-corrected.

Firstly, the cyclic and linear sweep voltammetry (CV and LSV) was recorded in the N₂- or O₂-saturated 1 M KOH electrolyte at a scan rate of 5 mV s⁻¹. The ORR LSV curves were tested at different rotating speeds (225-2025 rpm) and the OER polarization curves were performed at a rotating speed of 1600 rpm in the O₂-saturated electrolyte. Electrochemical impedance spectroscopy (EIS) measurements were conducted in the frequency range from 1×10⁶ to 0.1 Hz, at 0.85 V vs RHE. The electrical double-layer capacitance (C_{dl}) were estimated by CV curves within 1.048-1.148 V (vs RHE) at different scan rates. The chronopotentiometry curves were performed at the current density of 2 mA cm⁻² for ORR and 10 mA cm⁻² for OER, respectively.

The electron transfer number (*n*) was calculated by the Koutecky-Levich equations (1-2):

$$\frac{1}{J} = \frac{1}{J_L} + \frac{1}{J_K} = \frac{1}{B\omega^{1/2}} + \frac{1}{J_K} \quad (1)$$

$$B = 0.62nFC_0D_0^{3/2}\nu^{-1/6} \quad (2)$$

where J is the measured current density, J_L is the diffusion-limited current density, J_K is the kinetic current density, ω is the rotating speed, F is the Faraday constant (96485 C mol^{-1}), C_0 is the bulk concentration of O_2 ($1.2 \times 10^{-3} \text{ mol cm}^{-3}$), D_0 is the diffusion coefficient of O_2 ($1.9 \times 10^{-5} \text{ cm}^2 \text{ s}^{-1}$) and ν is the kinetic viscosity of electrolyte ($0.01 \text{ cm}^2 \text{ s}^{-1}$).

Zn-air battery (ZAB) was assembled in a two-electrode system with the as-prepared catalyst as the cathode, a polished Zn foil as an anode, 6 M KOH with 0.2 M zinc acetate as an electrolyte and carbon cloth as charge collector. The ZAB performance was tested on a LAND CT2001A instrument in the ambient environment. The gel electrolyte for the flexible ZAB was prepared by mixing poly(vinyl alcohol) (PVA) powder with DI water at $80 \text{ }^\circ\text{C}$ under 120 min and then 6 M KOH and 0.2 M zinc acetate were added into the solution.

Supplementary Figures

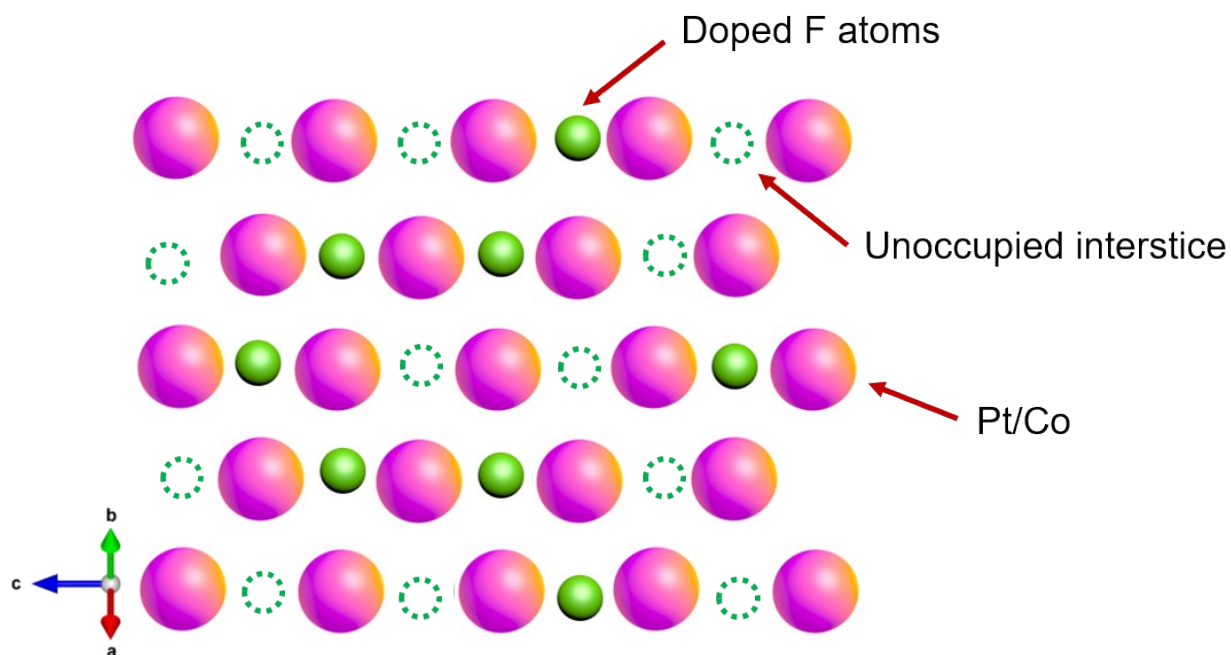


Figure S1. The atomic model of SA-PtCoF, the pink-golden color ball represents either Pt or Co atom in the first layer of SA-PtCoF. Note that the single Pt atoms are only coordinated with Co atoms instead of Pt atoms.

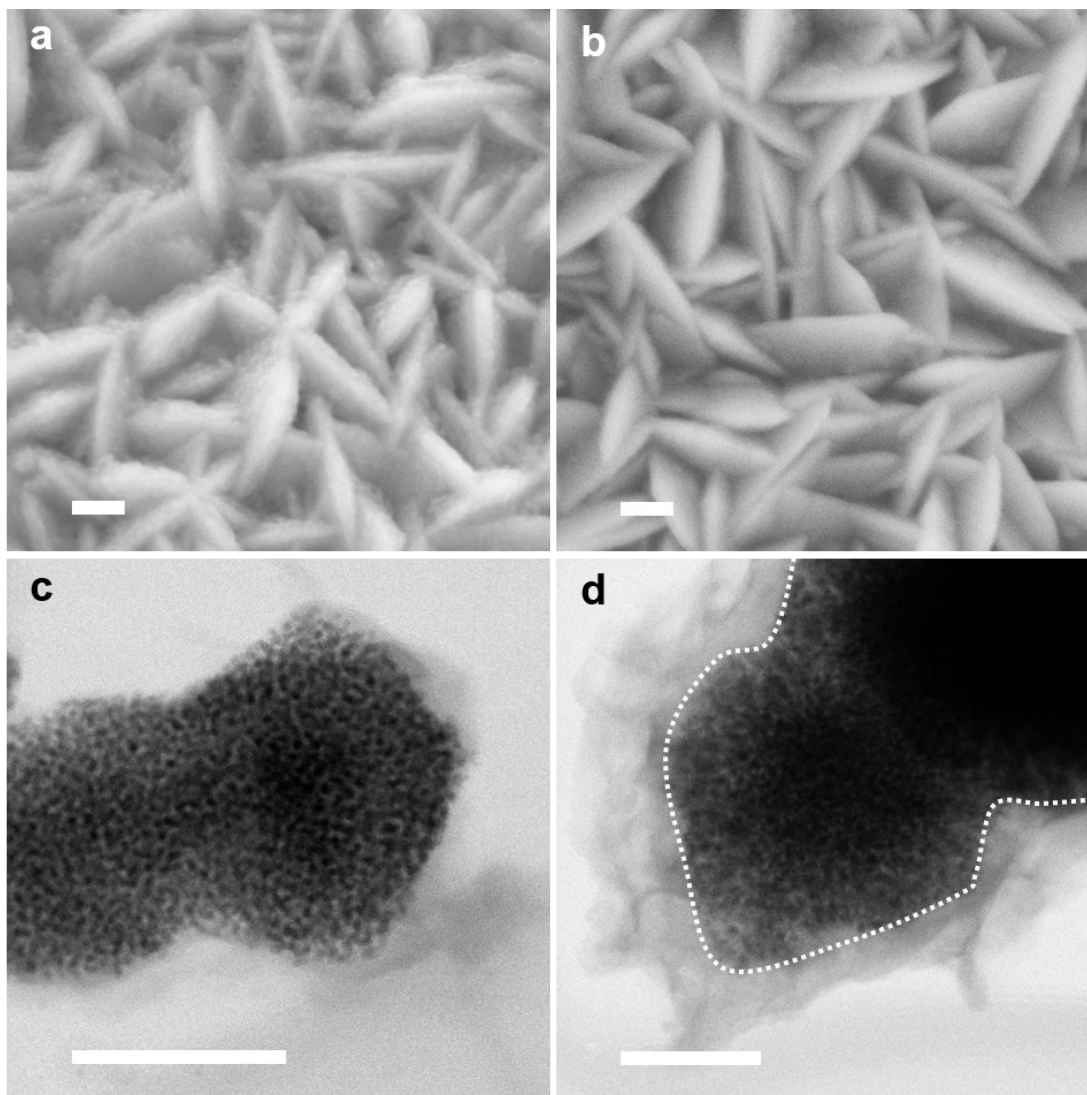


Figure S2. Morphology differences of the catalyst with and without F-plasma treatment, respectively. (a, b) SEM images of SA-PtCoF and PtCo, respectively. Scale bar, 200 nm. (c, d) ABF-STEM images of SA-PtCoF and PtCo, respectively. Scale bar, 50 nm.

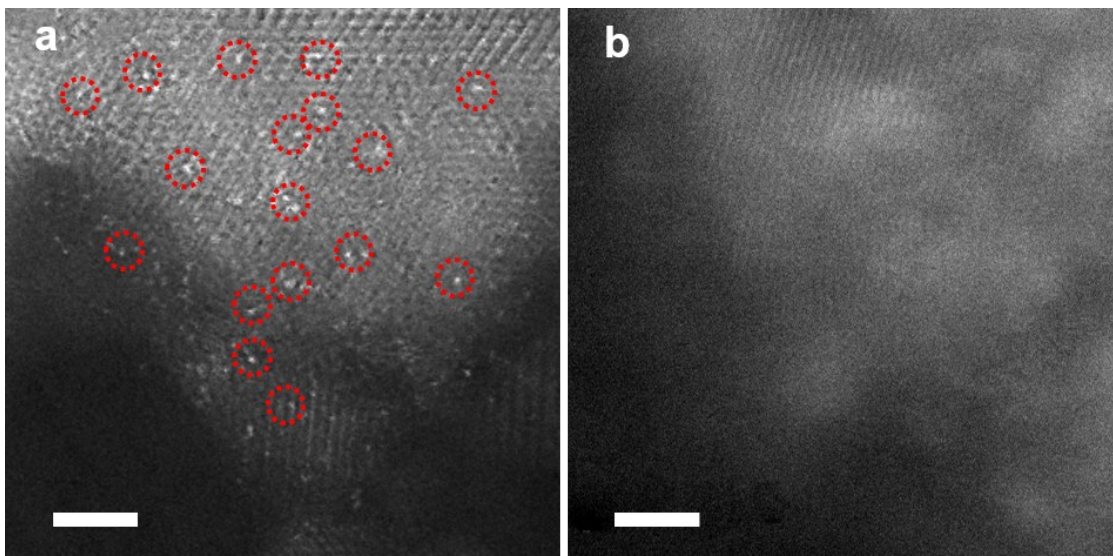


Figure S3. HAADF-STEM images of (a) SA-PtCoF and (b) PtCo catalysts, highlighting the atomic Pt on the edges marked by the red circles. Scale bar, 2 nm.

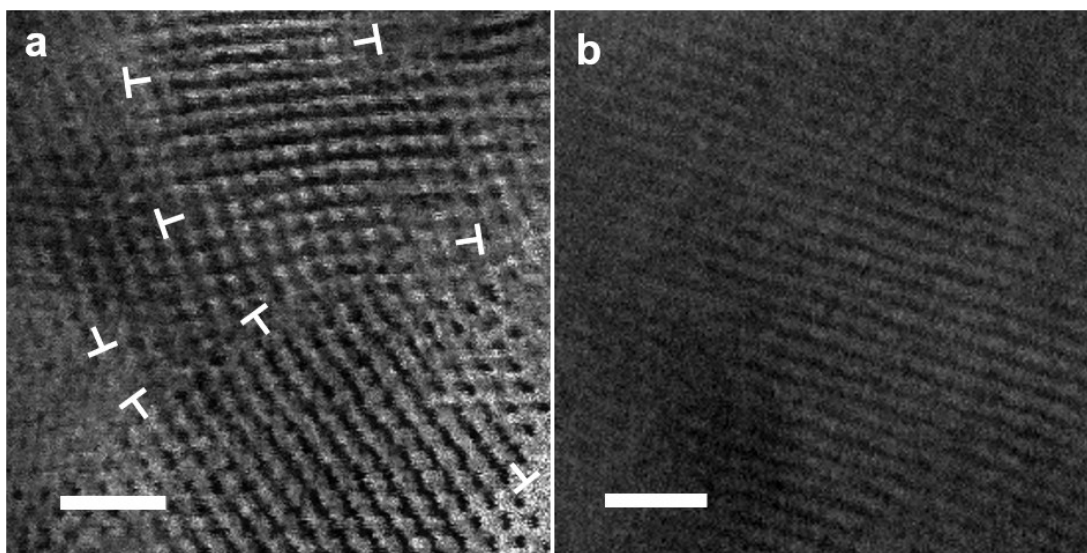


Figure S4. The high-resolution TEM images of matrixes (a) PtCoF and (b) PtCo from SA-PtCoF and PtCo catalysts, respectively. Scale bar, 1 nm. Lattice distortions are marked by red cycles and “T”.

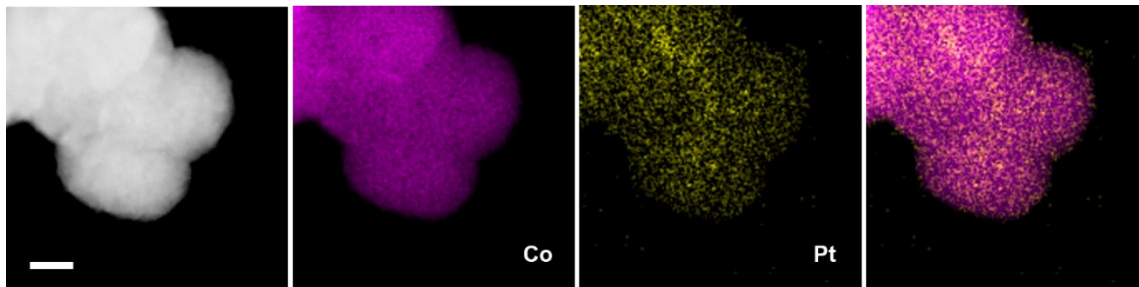


Figure S5. STEM-EDS element mapping of PtCo catalyst. Co and Pt distribute uniformly on the whole nanosheet. Scale bar, 100 nm.

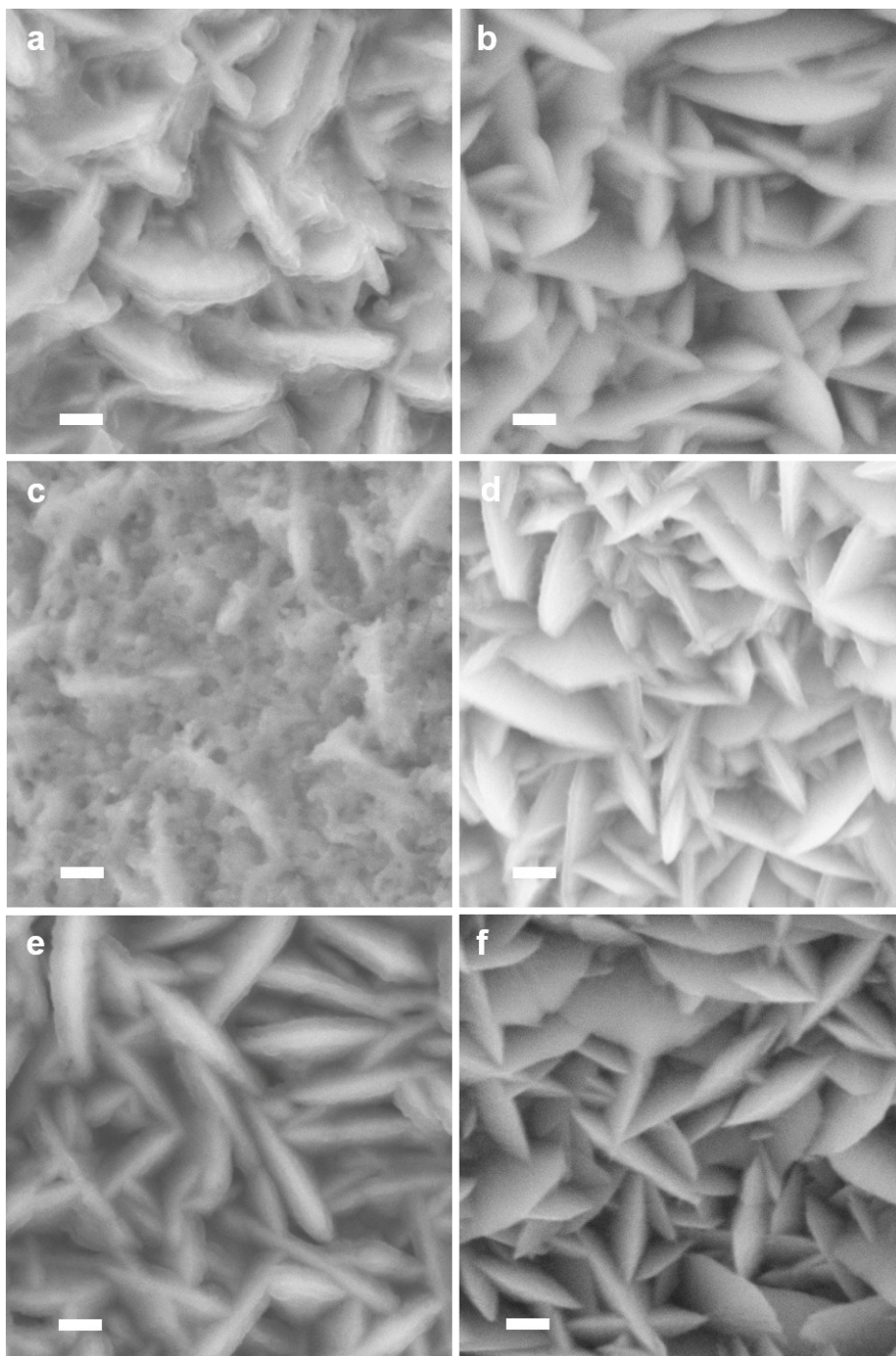


Figure S6. Morphologies of PtCo nanosheets with different concentration of Pt precursor with and without F-plasma treatment. SEM images of (a, b) AP-PtCoF and its corresponding nanosheets without F-plasma treatment. (c, d) NC-PtCoF and the corresponding nanosheets without F-plasma treatment, and (e, f) CoF and Co nanosheets. Scale bar, 200 nm.

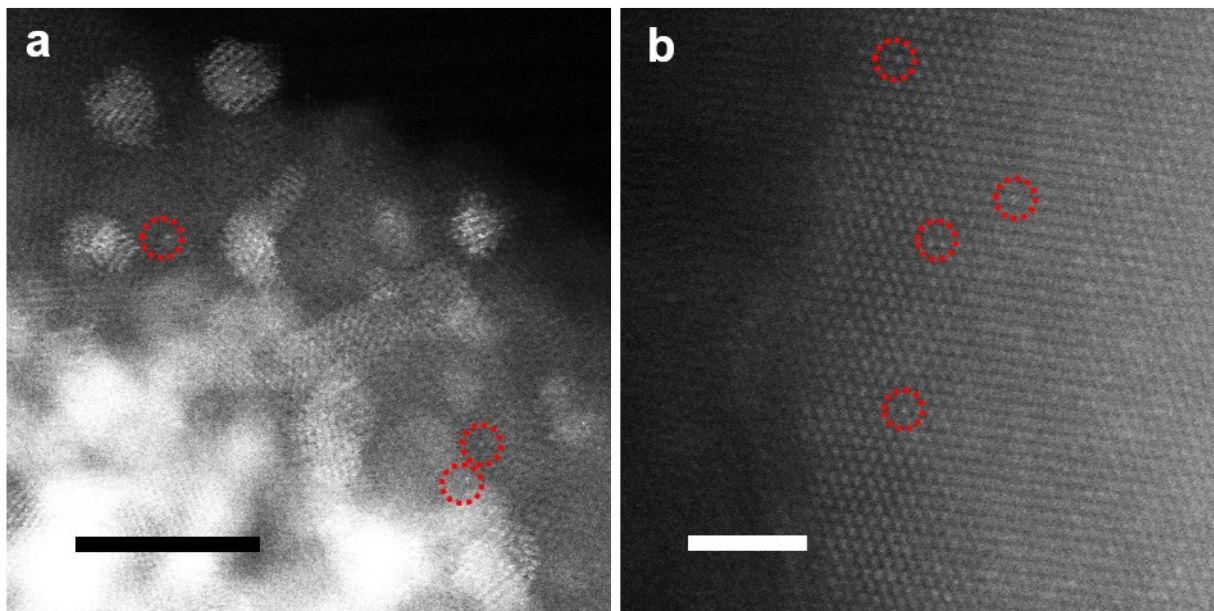


Figure S7. HAADF-STEM images of (a) NC-PtCoF, and (b) AP-PtCoF catalysts, highlighting the atomic Pt on the edges marked by the red circles. Scale bar, 5 nm, and 2 nm, respectively.

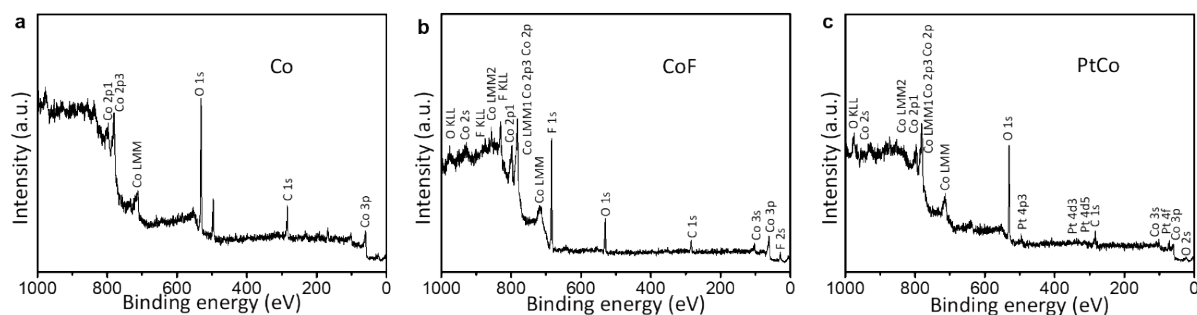


Figure S8. XPS survey spectra of (a) Co, (b) CoF, (c) PtCo.

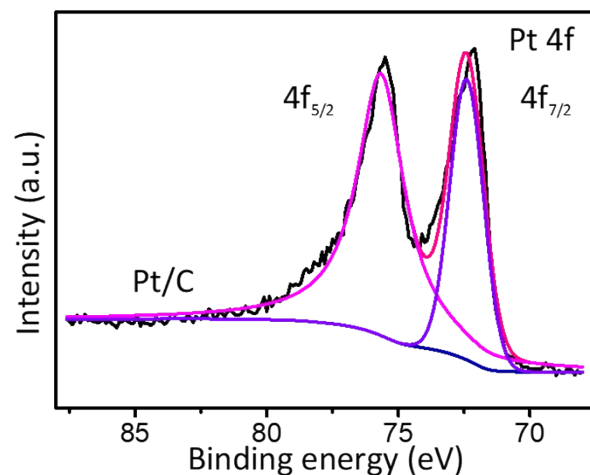


Figure S9. High-resolution XPS of Pt/C.

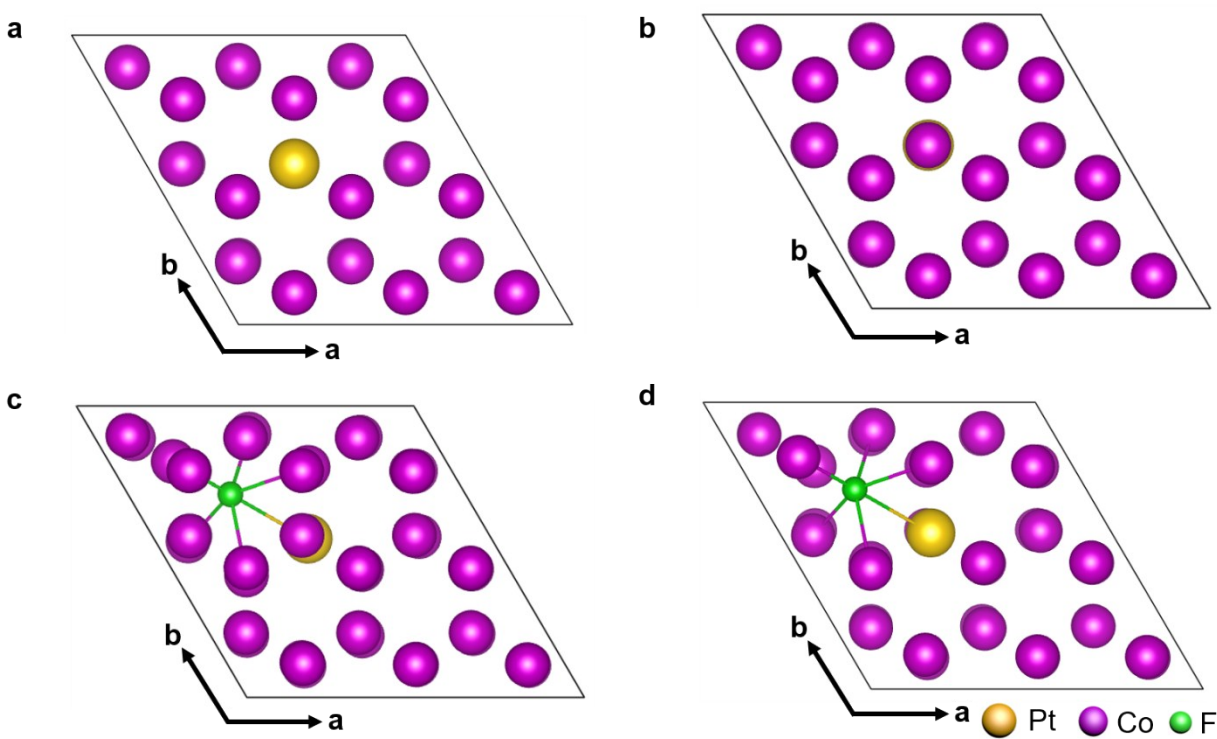


Figure S10. Configuration and top view of PtCo without (a, b) and with (c, d) interstitial F atom.

In order to show the location of Pt atom, the atoms of the top two layers were removed in (a, d).

The molar ratio of Co/Pt (53:1) agrees well with that in SA-PtCoF.

Table S1. Pt-Co nearest neighbor distance before and after inserting F.

	Bond length before inserting F (Å)	Bond length after inserting F (Å)
Pt-Co12	2.49	2.47
Pt-Co30	2.49	2.49
Pt-Co23	2.49	2.49
Pt-Co18	2.49	2.53
Pt-Co10	2.49	2.53
Pt-Co36	2.49	2.55
Pt-Co21	2.49	2.55
Pt-Co29	2.49	2.57
Pt-Co34	2.49	2.67
Pt-Co27	2.49	2.67
Pt-Co35	2.49	2.77
Pt-Co28	2.49	2.77

Table S2. The vibrational frequency of Pt-atom for different systems.

System	F_x (THz)	F_z (THz)	F_z (THz)
PtCo without F	5.32	5.32	5.06
PtCo with F	4.85	4.19	4.10

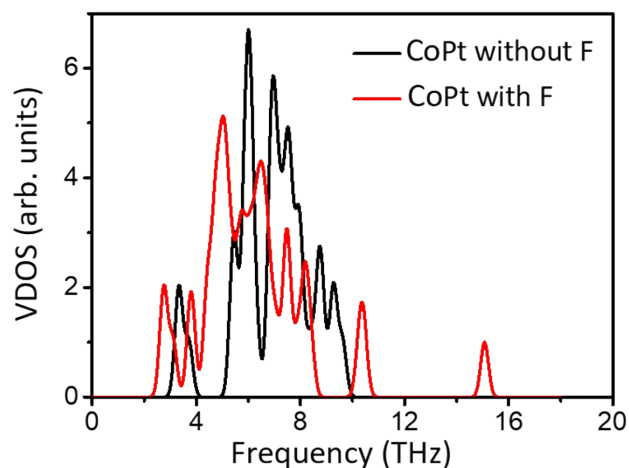


Figure S11. The vibrational density of states (VDOS) of CoPt system simulated based on SA-PtCoF model with and without F atoms calculated by density functional theory.

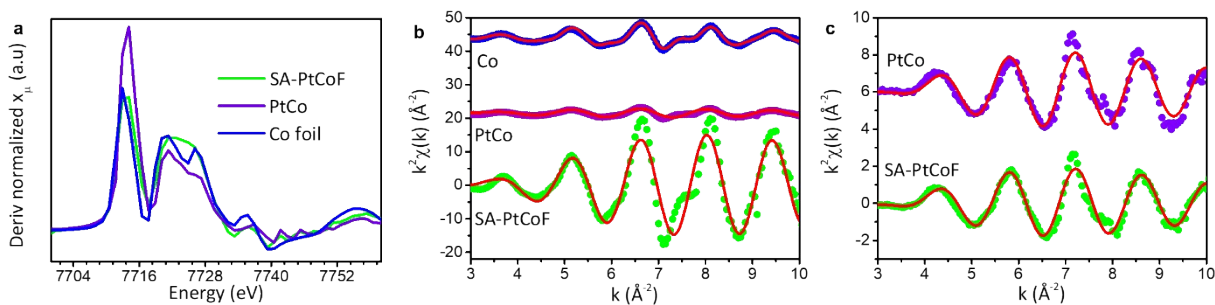


Figure S12. The XANES fitting results and EXAFS fitting results for Co, SA-PtCoF and PtCo samples. (a) Derivative of the normalized absorbance plotted against energy for Co-edge XANES (b) Co-edge EXAFS fitting results in k space (c) Pt-edge EXAFS fitting results in k space. For graphs b and c, circles represent the data and the solid red line represents the fit.

Table S3. EXAFS fitting results for Co metal, SA-PtCoF, and PtCo samples. CN, coordination number, R, the distance between the absorber and scatterer atoms, σ^2 , Debye-Waller factor to account for thermal and structural disorders, ΔE_0 , inner potential correction. EXAFS spectra of Pt and Co references are used to obtain the amplitude reduction factor S_0^2 values. Error bounds indicated in parenthesis are full errors for N and last digit errors for other parameters.

		CN	R(Å)	σ^2	ΔE_0 (eV)	R-factor
Co Edge	Co Metal					
	Co-Co1	8.8(0.9)	2.492(1)	0.006(5)		
	Co-Co3	4.4(0.6)	3.502(2)	0.010(1)		
	Co-Co5	13.2(1.2)	4.341(1)	0.007(7)	8.4(1)	0.008
	Co-Co7	8.8(1.0)	4.834(4)	0.003(3)		
	SA-PtCoF					
	Co-Co1	9.5(0.6)	2.639(6)	0.005(1)	-9.9(1)	0.023
	PtCo					
	Co-Co1	6.0(0.5)	2.643(5)	0.005(1)	-9.9(1)	0.022
	Pt Edge	SA-PtCoF				
Pt-Co1		7.4(0.9)	2.562(3)	0.006(1)	7.5(3)	0.017
PtCo						
	Pt-Co1	7.9(1.0)	2.554(8)	0.005(1)	8.5(4)	0.025

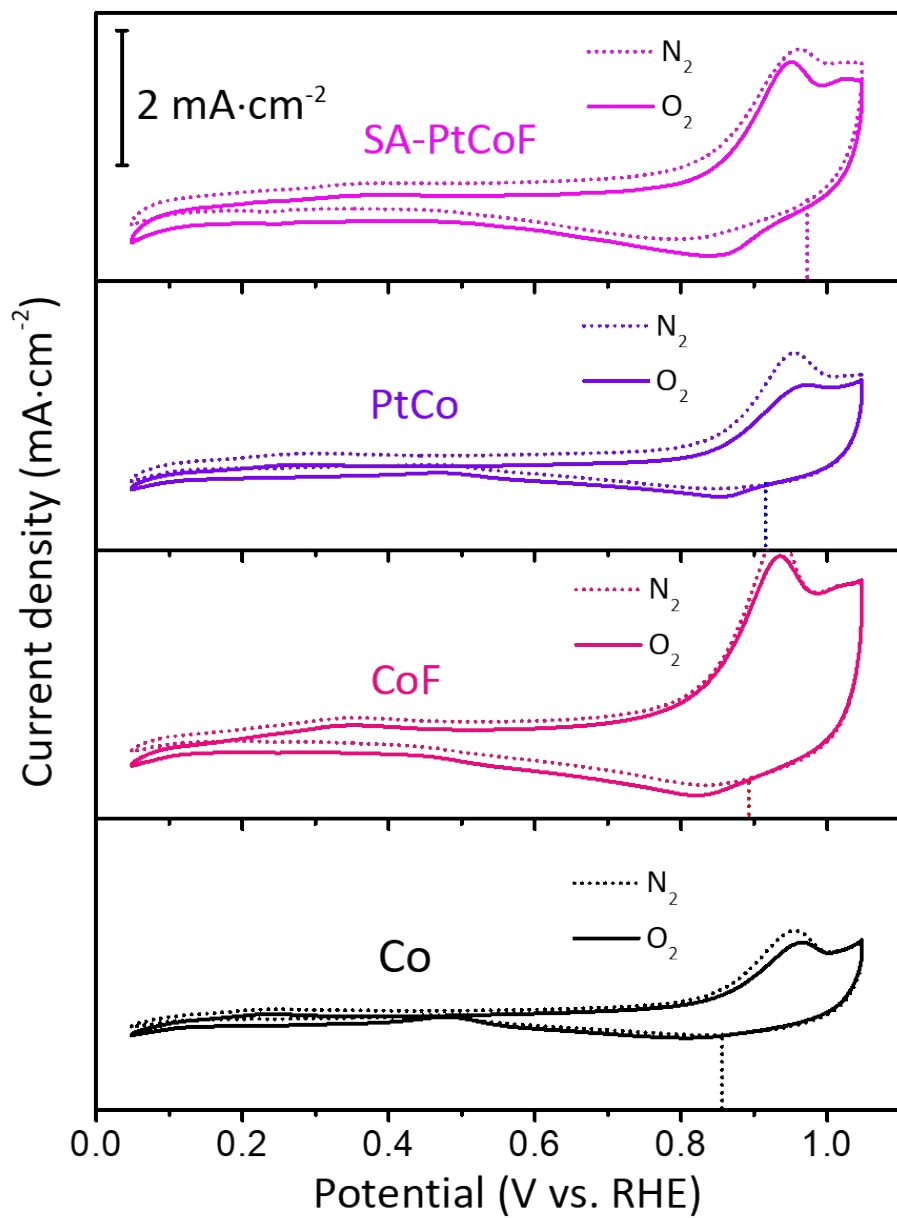


Figure S13. CV curves of the catalysts in the N_2 - and O_2 -saturated 1 M KOH.

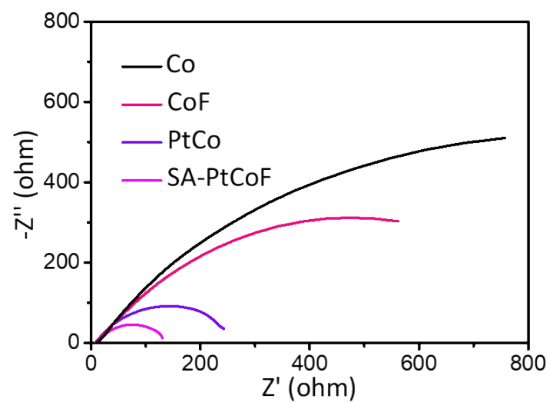


Figure S14. EIS of Co, CoF, PtCo, and SA-PtCoF catalysts in O₂-saturated 1 M KOH at 0.85 V.

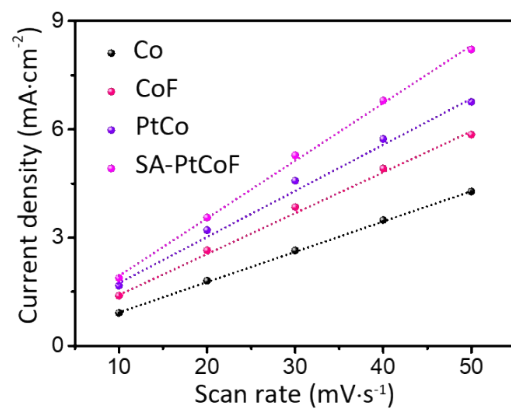


Figure S15. Capacitive current densities as a function of scan rate for SA-PtCoF, PtCo, CoF, and Co catalysts in 1 M KOH.

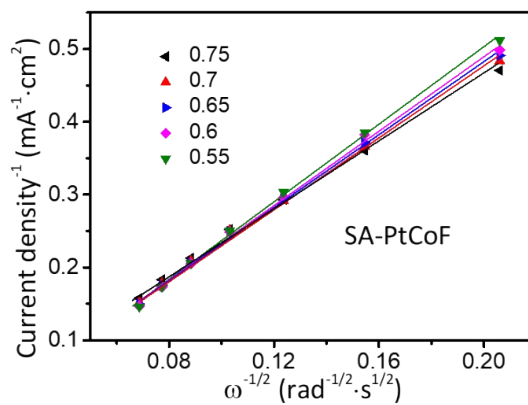


Figure S16. K-L plots for SA-PtCoF.

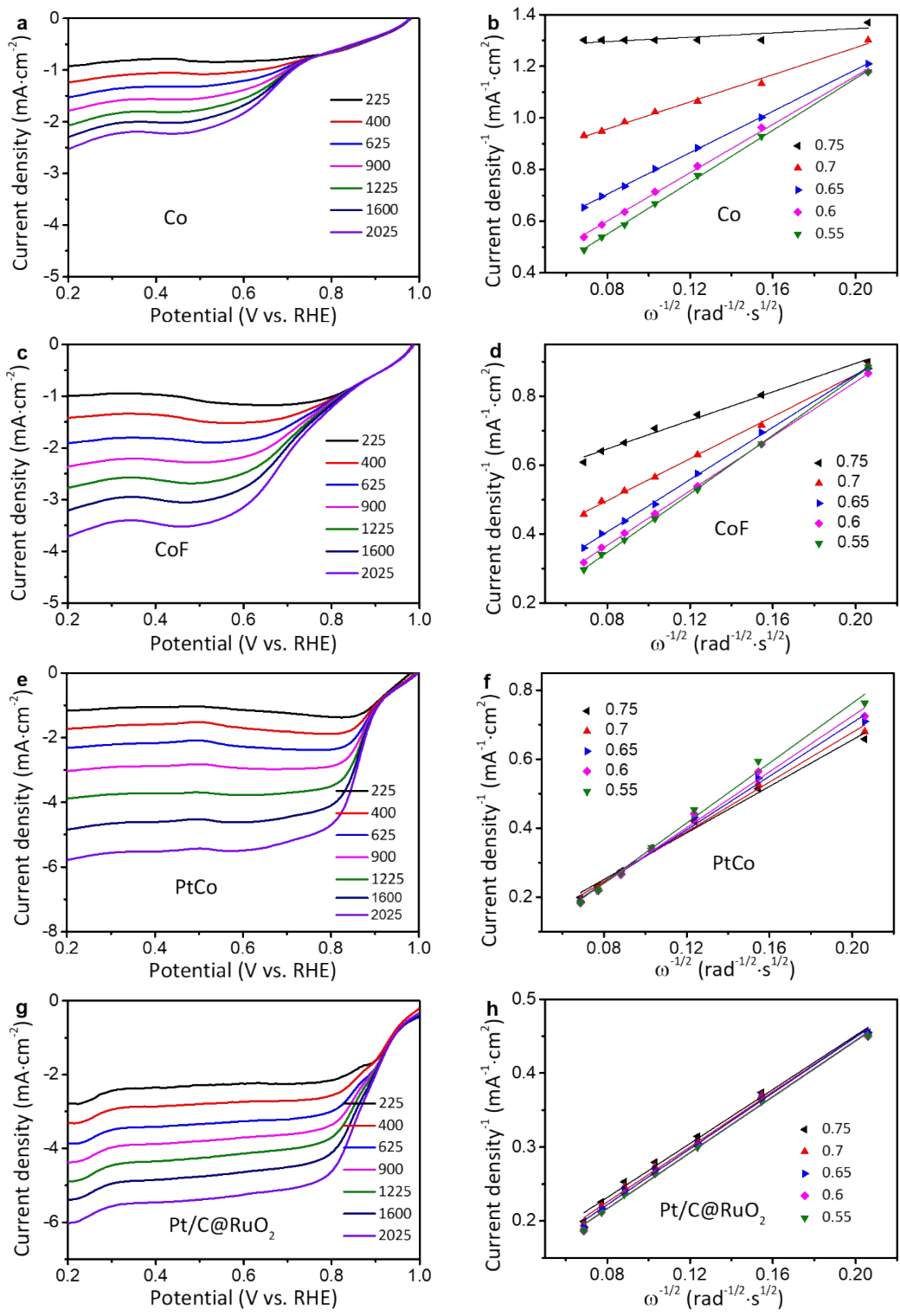


Figure S17. ORR polarization curves and the corresponding K-L plots for the control samples.

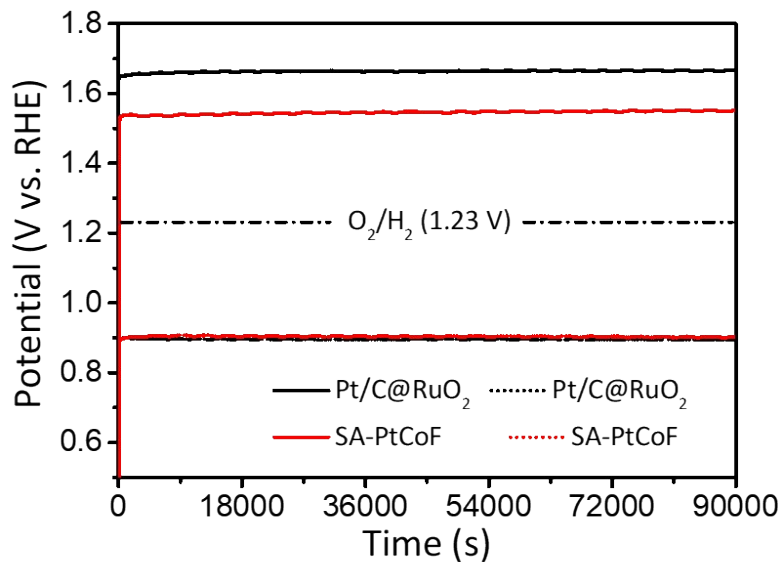


Figure S18. Chronopotentiometry curves for SA-PtCoF and Pt/C@RuO₂ tested in 1 M KOH.

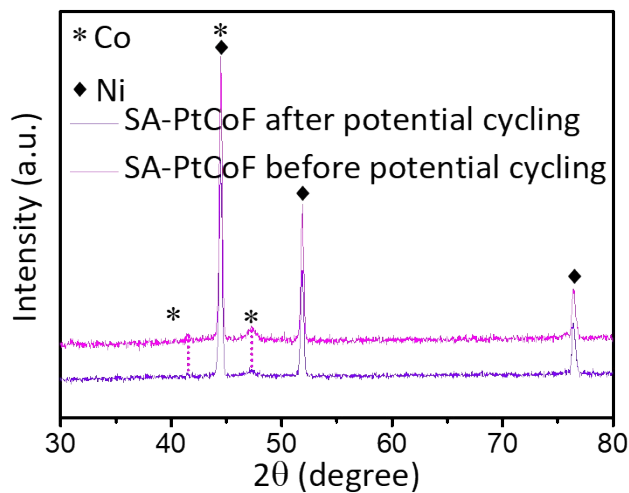


Figure S19. XRD patterns of SA-PtCoF before and after the cycling test.

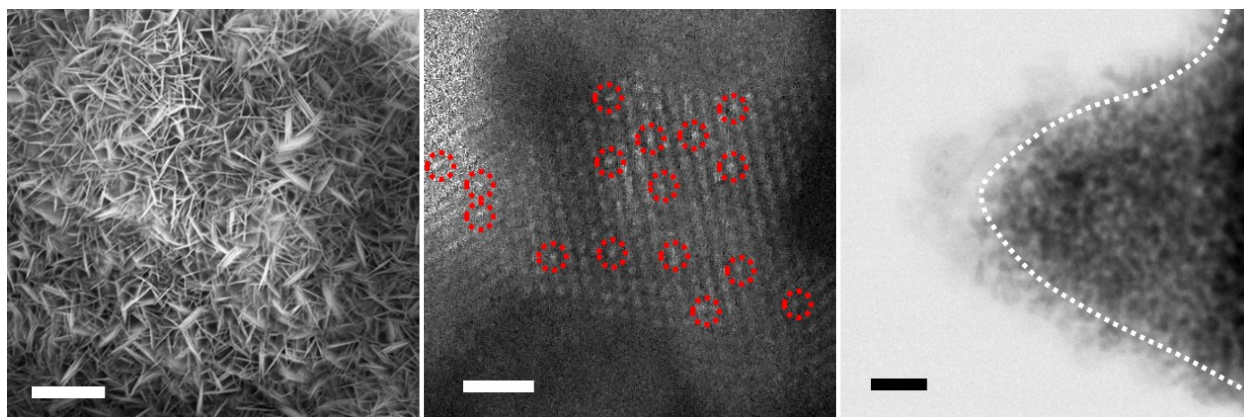


Figure S20. The structural stability of SA-PtCoF after cycling test. (a) SEM image of SA-PtCoF nanosheets grown on the nickel foam. Scale bar, 1 μm . (b) HAADF-STEM image and (c) ABF-STEM image of SA-PtCoF. Scale bar, 1 nm, and 10 nm, respectively. Highlight that the atomic Pt on the edges marked by the red circles.

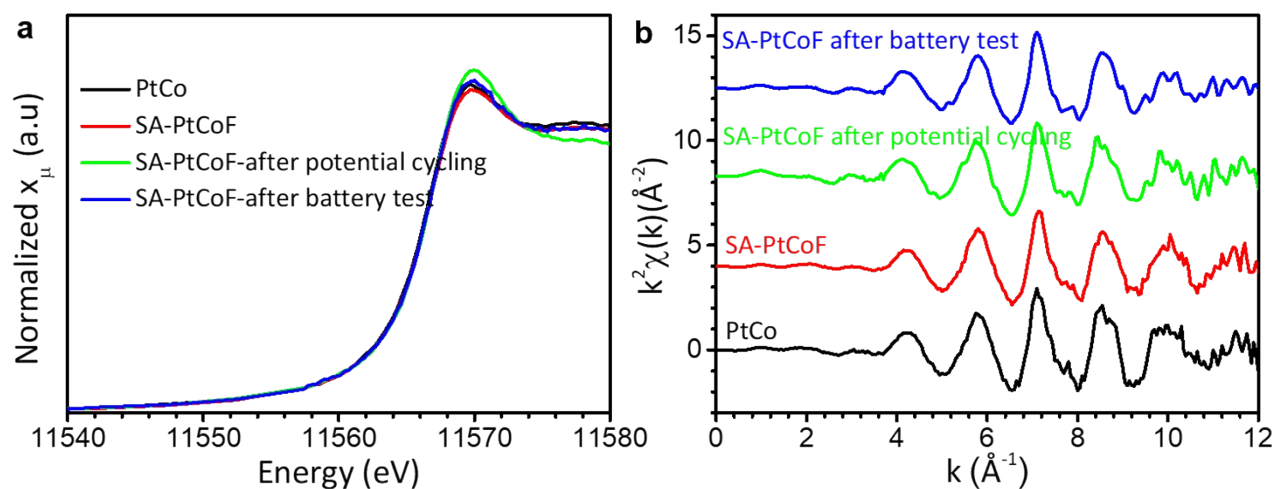


Figure S21. Pt L₃-edge spectra (a) XANES (b) EXAFS K-space for PtCo, SA-PtCoF, SA-PtCoF after potential cycling test, and SA-PtCoF after battery cycling.

Table S4. The list of the weight percentages of Pt before measurement, after long-life electrochemical test and zinc-air battery cycling recorded by XRF.

SA-PtCoF	Pt weight percentage (wt %)
Before reactions	5.86
After the long-life cycling	5.81
After ZAB battery cycling	5.85

Table S5. ORR and OER activities of SA-PtCoF catalyst compared to the state-of-the-art catalysts.

Catalysts	ORR- $E_{1/2}$ (V vs RHE)	OER- $E_{1/2}$ (V vs RHE)	$\Delta E = E_{j10} - E_{1/2}$ (V vs RHE)	Mass loading ($\mu\text{g cm}^{-2}$)	Ref.
SA-PtCoF	0.88	1.54	0.66	420	This work
Co@NG-acid	0.83	-	-	380	1
CoPt-9/DTM-C	0.81	1.61	0.80	40.8	2
NC-Co SA	0.87	1.59	0.72	1350	3
Pt ₁ @Fe-N-C	0.80	1.54	0.74	400	4
Pt1/ATO	0.56	> 1.90	> 1.34	400	5
Pt 20 s/SC CoO NRs	0.87	1.58	0.71	400	6
Co(OH) ₂ /CoPt/N-CN	0.83	1.55	0.72	120	7
Pt ₁ -N/BP	0.87	-	-	-	8
FeCo/N-DNC	0.81	1.62	0.81	102	9
Co@Pt-NC	0.87	-	-	-	10

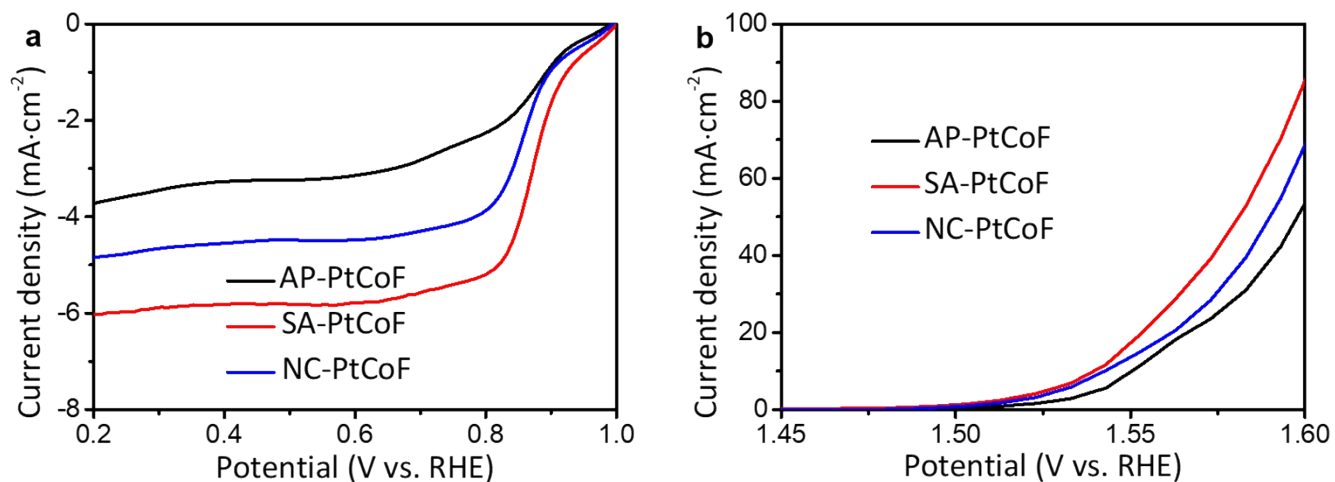


Figure S22. The ORR and OER polarization curves for PtCoF catalysts with different Pt weight percentages (1.85 wt%, 5.87 wt%, and 6.21 wt%) corresponding to AP-PtCoF, SA-PtCoF, and NC-PtCoF, respectively.

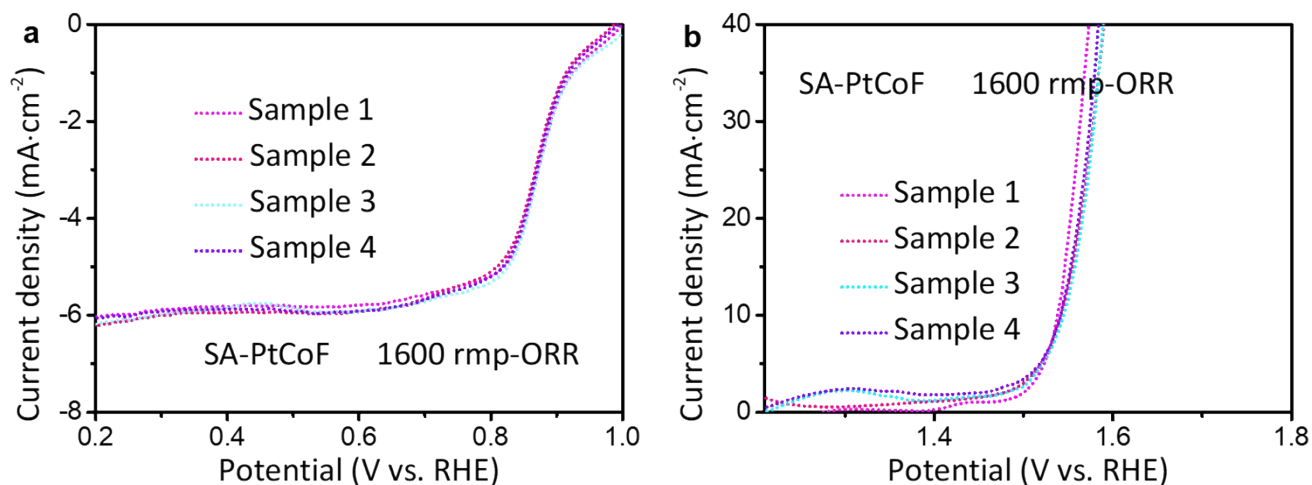


Figure S23. Repeatable performances of ORR and OER tested by using the SA-PtCoF catalysts fabricated at different batches.

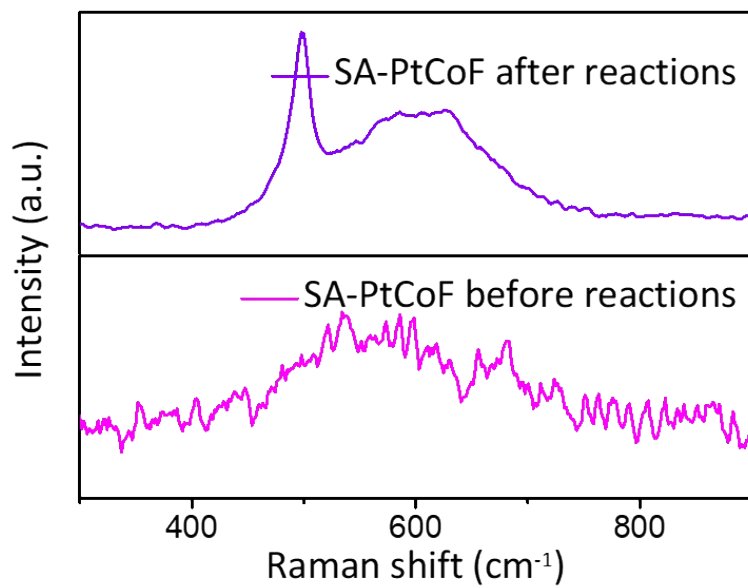


Figure S24. The Raman spectrum of SA-PtCoF before and after ORR and OER.

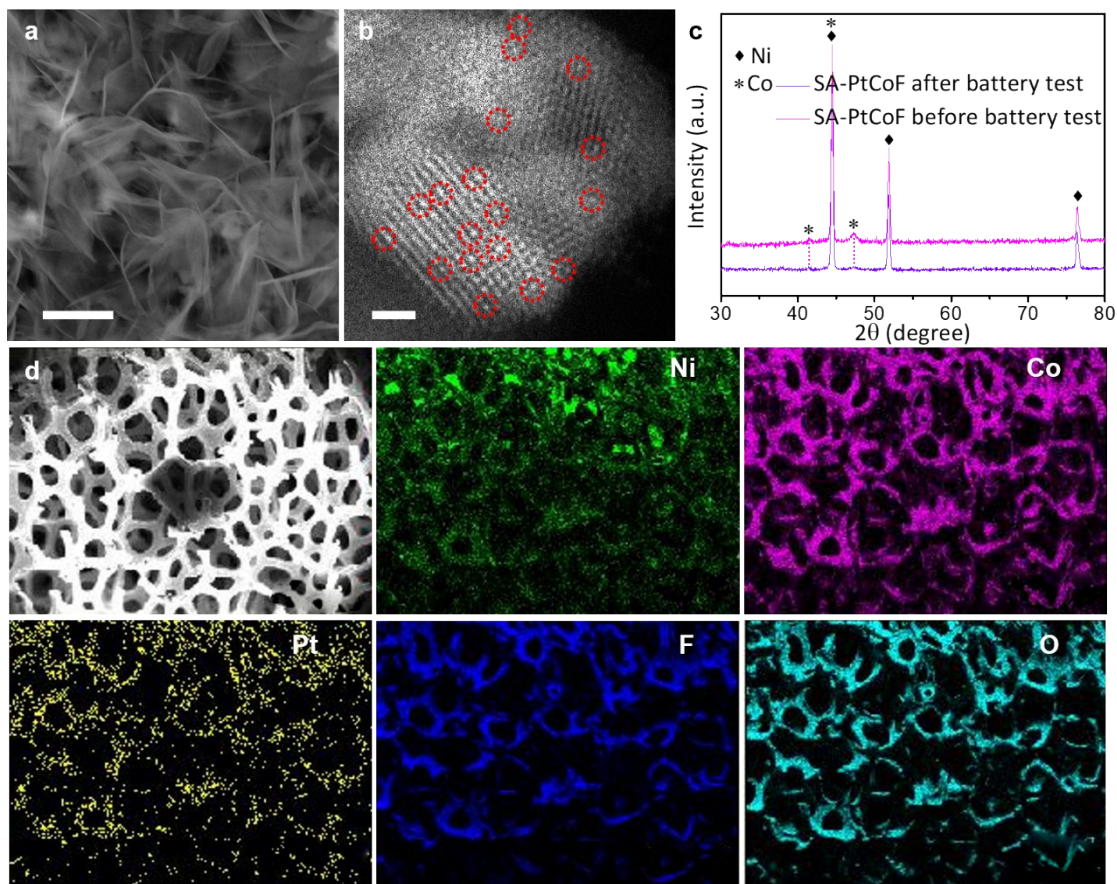


Figure S25. The characterization of SA-PtCoF after long discharge/charge cycling in ZAB. (a) SEM image of SA-PtCoF nanosheets grown on nickel foam and (b) HAADF-STEM images of SA-PtCoF after long cycling test, highlighting the atomic Pt on the edges marked by the red circles. Scale bar, 1 μm and 1nm, respectively. (c) The contrast of the XRD patterns of SA-PtCoF before and after long term durability test. (d) EDS elemental mapping of SA-PtCoF after testing. Scale bar, 500 μm.

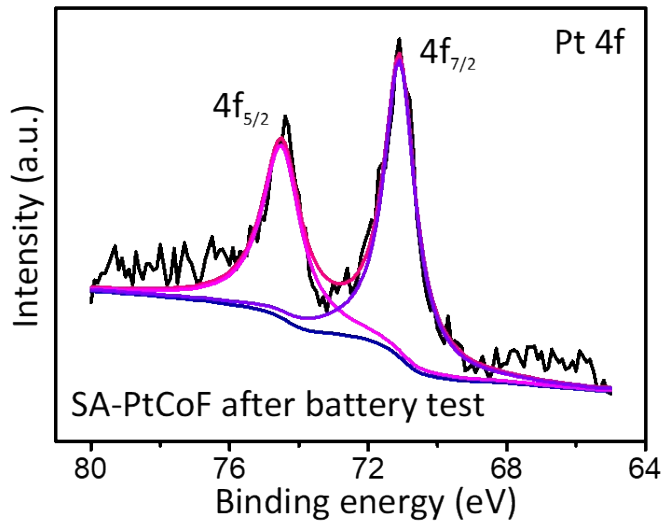


Figure S26. High-resolution XPS of SA-PtCoF as the cathode material after the discharge and charge cycling in ZAB.

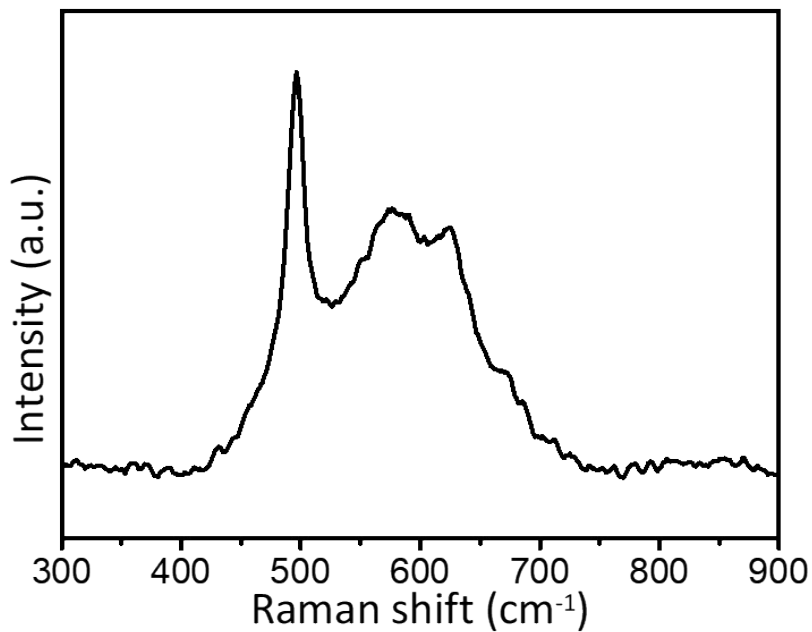


Figure S27. The Raman spectrum of SA-PtCoF as the cathode material in ZAB after the discharge and charge cycling.

Table S6. Battery performance of SA-PtCoF compared to the benchmarking ZABs.

Catalyst	Power density (mW cm ⁻²)	Ref.
SA-PtCoF	125	This work
NC-Co SA	20.9	3
Pt1/ATO	36	5
FeCo/N-DNC	115	9
Co/Co ₃ O ₄ @PGS	118.27	11
CoN ₄ /NG	115	12
CoNi@NCNT/NF	108	13
mPtPd-NF	108	14

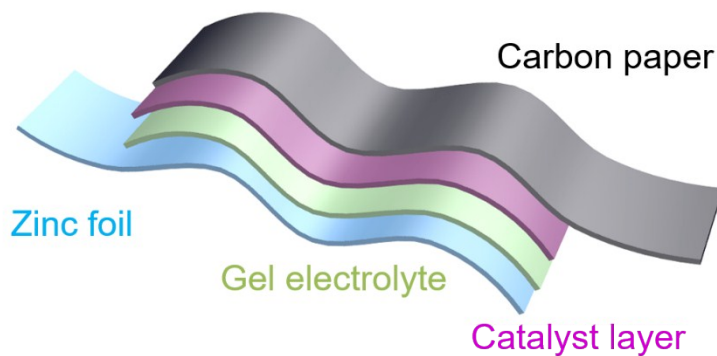


Figure S28. The configuration of the flexible rechargeable ZAB.



Figure S29. The open-circuit potential (OCP) of the flexible rechargeable ZAB.

Reference

1. M. Zeng, Y. Liu, F. Zhao, K. Nie, N. Han, X. Wang, W. Huang, X. Song, J. Zhong and Y. Li, *Adv. Funct. Mater.*, 2016, **26**, 4397-4404.
2. K. Wang, Z. Tang, W. Wu, P. Xi, D. Liu, Z. Ding, X. Chen, X. Wu and S. Chen, *Electrochim. Acta*, 2018, **284**, 119-127.
3. W. Zang, A. Sumboja, Y. Ma, H. Zhang, Y. Wu, S. Wu, H. Wu, Z. Liu, C. Guan, J. Wang and S. J. Pennycook, *ACS Catal.*, 2018, **8**, 8961-8969.
4. X. Zeng, J. Shui, X. Liu, Q. Liu, Y. Li, J. Shang, L. Zheng and R. Yu, *Adv. Energy Mater.*, 2018, **8**, 1701345.
5. J. Kim, C.-W. Roh, S. K. Sahoo, S. Yang, J. Bae, J. W. Han and H. Lee, *Adv. Energy Mater.*, 2018, **8**, 1701476.
6. C. Meng, T. Ling, T. Y. Ma, H. Wang, Z. Hu, Y. Zhou, J. Mao, X. W. Du, M. Jaroniec and S. Z. Qiao, *Adv. Mater.*, 2017, **29**, 1604607.
7. K. Wang, W. Wu, Z. Tang, L. Li, S. Chen and N. M. Bedford, *ACS Appl. Mater. Interfaces*, 2019, **11**, 4983-4994.
8. J. Liu, M. Jiao, L. Lu, H. M. Barkholtz, Y. Li, Y. Wang, L. Jiang, Z. Wu, D. J. Liu, L. Zhuang, C. Ma, J. Zeng, B. Zhang, D. Su, P. Song, W. Xing, W. Xu, Y. Wang, Z. Jiang and G. Sun, *Nat. Commun.*, 2017, **8**, 15938.
9. G. Fu, Y. Liu, Y. Chen, Y. Tang, J. B. Goodenough and J. M. Lee, *Nanoscale*, 2018, **10**, 19937-19944.
10. L. Wang, Z. Tang, W. Yan, Q. Wang, H. Yang and S. Chen, *J. Power Sources*, 2017, **343**, 458-466.
11. Y. Jiang, Y.-P. Deng, J. Fu, D. U. Lee, R. Liang, Z. P. Cano, Y. Liu, Z. Bai, S. Hwang, L. Yang, D. Su, W. Chu and Z. Chen, *Adv. Energy Mater.*, 2018, **8**, 1702900.
12. L. Yang, L. Shi, D. Wang, Y. Lv and D. Cao, *Nano Energy*, 2018, **50**, 691-698.
13. W. Niu, S. Pakhira, K. Marcus, Z. Li, J. L. Mendoza-Cortes and Y. Yang, *Adv. Energy Mater.*, 2018, **8**, 1800480.
14. H. Wang, H. Yu, S. Yin, Y. Xu, X. Li, H. Xue and L. Wang, *ACS Sustain. Chem. Eng.*, 2018, **6**, 12367-12374.